

1 **Particle number concentrations and size distributions in the stratosphere: Implications of
2 nucleation mechanisms and particle microphysics**

3 Fangqun Yu¹, Gan Luo¹, Arshad Arjunan Nair¹, Sebastian Eastham^{2,3}, Christina J. Williamson⁴,
4 ^{5, a}, Agnieszka Kupc^{5,6}, and Charles A. Brock⁵

5 ¹ Atmospheric Sciences Research Center, University at Albany, Albany, New York, US

6 ² Laboratory for Aviation and the Environment, Department of Aeronautics and Astronautics,
7 Massachusetts Institute of Technology, Cambridge, MA 02139, USA

8 ³ Joint Program on the Science and Policy of Global Change, Massachusetts Institute of
9 Technology, Cambridge, MA 02139, USA

10 ⁴ Cooperative Institute for Research in Environmental Sciences, University of Colorado,
11 Boulder, CO 80309, USA

12 ⁵ Chemical Sciences Laboratory, National Oceanic and Atmospheric Administration, Boulder,
13 CO 80305, USA

14 ⁶ Faculty of Physics, Aerosol Physics and Environmental Physics, University of Vienna, 1090
15 Vienna, Austria

16 ^a now at: Climate Research Programme, Finnish Meteorological Institute, 00101 Helsinki,
17 Finland and Institute for Atmospheric and Earth System Research/Physics, Faculty of Science,
18 University of Helsinki, 00014 Helsinki, Finland.

19

20 Correspondence to: F. Yu (fyu@albany.edu)

21

22 **Abstract.** While formation and growth of particles in the troposphere have been extensively
23 studied in the past two decades, very limited efforts have been devoted to understanding these in
24 the stratosphere. Here we use both Cosmics Leaving OUtdoor Droplets (CLOUD) laboratory
25 measurements taken under very low temperatures (205–223K) and Atmospheric Tomography
26 Mission (ATom) in-situ observations of particle number size distributions (PNSD) down to 3 nm
27 to constrain nucleation mechanisms and to evaluate model simulated particle size distributions in
28 the lowermost stratosphere (LMS). We show that the binary homogenous nucleation (BHN)
29 scheme used in most of the existing stratospheric aerosol injection (a proposed method of solar
30 radiation modification) modeling studies overpredict the nucleation rates by 3–4 orders of

31 magnitude (when compared to CLOUD data) and particle number concentrations in the
32 background LMS by a factor ~2–4 (when compared to ATom data). Based on a recently developed
33 kinetic nucleation model, which gives rates of both ion-mediated nucleation (IMN) and BHN at
34 low temperatures in good agreement with CLOUD measurements, both BHN and IMN occur in
35 the stratosphere. However, IMN rates are generally more than one order of magnitude higher than
36 BHN rates and thus dominate nucleation in the background stratosphere. In the Southern
37 Hemisphere (SH) LMS with minimum influence of anthropogenic emissions, our analysis shows
38 that ATom measured PNSDs generally have four apparent modes. The model captures reasonably
39 well the two modes (Aitken mode and the first accumulation mode) with the highest number
40 concentrations and the size-dependent standard deviations. However, the model misses an apparent
41 second accumulation mode peaking around 300–400 nm, which is in the size range important for
42 aerosol direct radiative forcing. The bi-modal structure of accumulation mode particles has also
43 been observed in the stratosphere well above tropopause and in the volcano-perturbed stratosphere.
44 We suggest that this bi-modal structure may be caused by the effect of charges on coagulation and
45 growth, which is not yet considered in any existing models and may be important in the
46 stratosphere due to high ionization rates and long lifetime of aerosols. Considering the importance
47 of accurate PNSDs for projecting realistic radiation forcing response to stratospheric aerosol
48 injection (SAI), it is essential to understand and incorporate such potentially important processes
49 in SAI model simulations.

50

51

52

Deleted: e

Deleted: e

55 **1. Introduction**

56 Solar radiation modification (also known as solar geoengineering) approaches are being
57 developed in response to the climate crisis (IPCC, 2021). They would temporarily offset climate
58 change by reducing incoming sunlight, augmenting (currently inadequate) mitigation efforts and
59 buying time to reduce atmospheric levels of CO₂, which is the root cause of the climate crisis. A
60 recent report by the National Academies of Sciences, Engineering and Medicine (NASEM)
61 emphasizes the urgent need to have a comprehensive understanding of the feasibility and potential
62 risks/benefits of solar climate intervention approaches (NASEM, 2021). Stratospheric aerosol
63 injection (SAI) has demonstrated the most promise as proximately engineerable (Shepherd et al.,
64 2009; Lockley et al., 2020; IPCC, 2021) and has been extensively studied using models (e.g.,
65 GeoMIP: Kravitz et al., 2011; GLENS: Mills et al., 2017; Richter et al., 2022). The NASEM report
66 (NASEM, 2021) pointed out that “the overall magnitude and spatial distribution of the forcing
67 produced by SAI depends strongly on the aerosol size distribution” and “One of the research
68 priorities for SAI is thus to address critical gaps in knowledge about the evolution of the aerosol
69 particle size distribution”. In the stratosphere, sulfate aerosols are formed by nucleation, followed
70 by condensational growth and coagulation, and lost by evaporation in the upper stratosphere and
71 downward sedimentation into the troposphere (Turco et al., 1982). New particle formation (NPF)
72 (or nucleation) affects not only the number abundance but also the size distributions of
73 stratospheric particles (e.g., Brock et al., 1995; Lee et al., 2003). There is increasing evidence
74 (Weisenstein et al., 2022; Laakso et al., 2022) that a careful treatment of microphysical processes
75 is necessary for projecting realistic radiative forcing response to SAI.

76 The process of NPF under tropospheric conditions has been extensively explored over the last
77 two decades through laboratory and field measurements, theoretical studies, and numerical
78 simulations (e.g., Yu and Turco, 2000; Vehkamäki et al., 2002; Kulmala et al., 2004; Kirkby et al.,
79 2011; Dawson et al., 2012; Zhang et al., 2012; Kürten et al., 2016; Yu et al., 2018; Kerminen et
80 al., 2018; Lee et al., 2019). Although some of the advances in our understanding of nucleation
81 gained in the last two decades can be applied to stratospheric conditions, focused studies
82 specifically examining the mechanisms of NPF under stratospheric conditions are quite limited.
83 Indeed, the H₂SO₄–H₂O binary homogenous nucleation (BHN) parameterization developed two
84 decades ago by Vehkamäki et al. (2002) (named BHN_V2002 thereafter) has been widely used in
85 SAI modeling studies when nucleation process is explicitly considered (e.g., Tilmes et al., 2015;
86 Jones et al., 2021; Weisenstein et al., 2022). Tilmes et al. (2015) described a Geoengineering
87 Model Intercomparison Project (GeoMIP) experiment designed for climate and chemistry models,
88 using the stratospheric aerosol distribution derived from the ECHAM5-HAM microphysical model
89 (Stier et al., 2005) which calculated nucleation rates with the BHN_V2002 scheme. Both models
90 (UKESM1 and CESM2-WACCM6) employed for a recent GeoMIP G6sulfur study (Jones et al.,
91 2021) used the BHN_V2002 scheme. In another recent SAI study based on three interactive
92 stratospheric aerosol microphysics models (Weisenstein et al., 2022), two models (MAECHAM5-
93 HAM and SOCOL-AER) used BHN_V2002 scheme while the other (CESM2-WACCM) used an
94 empirical nucleation scheme to calculate nucleation rate as a function of sulfuric acid concentration
95 only (i.e. no dependence on temperature and relative humidity).

To our knowledge, the
96 performance of this widely used BHN_V2002 under stratospheric conditions has not been
97 carefully examined, probably due to the lack of suitable in situ measurements of freshly nucleated
98 particles in the stratosphere for constraining the scheme. In this regard, particle size distributions
99 down to 3 nm measured in-situ during the NASA Atmospheric Tomography Mission (ATom) in

Deleted: used in most of SAI modeling studies when
nucleation mechanism is considered (e.g., Weisenstein et al.,
2022, Laakso et al., 2022)

103 the lowermost stratosphere (LMS) of both SH and NH in four different seasons (Williamson et al.,
104 2019, 2021; Kupc et al., 2020; Brock et al., 2021) provide much-needed data to constrain our
105 understanding of the nucleation and particle microphysics in the stratosphere. In addition, well-
106 controlled CLOUD experiments taken under low temperature (within the range of stratosphere)
107 can also be used to assess the performance of nucleation schemes under stratospheric conditions.
108 Another important issue related to stratospheric particles is the role of ionization in nucleation. It
109 is well established that nucleation of $\text{H}_2\text{SO}_4\text{--H}_2\text{O}$ on ions is favored over homogenous nucleation
110 (Hamill et al., 1982; Yu and Turco, 2000; Lovejoy et al., 2004; Kirkby et al. 2011; Yu et al., 2018)
111 but the role of ionization in NPF in the stratosphere has not been considered in any previous SAI
112 studies (to our knowledge) in spite of the very high ionization rates in the stratosphere.

113 In this study, we use both CLOUD laboratory measurements taken under very low
114 stratospheric temperatures and ATom PNSD measurements in LMS to constrain nucleation
115 mechanisms and model simulated particle size distributions. For 3-D simulation of size-resolved
116 stratospheric aerosols, we use the GEOS-Chem with the unified tropospheric-stratospheric
117 chemistry-transport model with the size-resolved advanced particle microphysics (APM) package.
118

119 **2. Model and data**

120 **2.1 GEOS-Chem/APM**

121 The GEOS-Chem model is a global 3-D model of atmospheric composition (e.g., Bey et al.,
122 2001) and is continuously being improved (e.g., Luo et al., 2020; Holmes et al., 2019; Keller et al.,
123 2014; Murray et al., 2012; Pye and Seinfeld, 2010; van Donkelaar et al., 2008; Evans and Jacob,
124 2005; Martin et al., 2003). The GEOS-Chem tropospheric–stratospheric unified chemistry
125 extension (UCX; Eastham et al., 2014), now the standard GEOS-Chem configuration, implements
126 stratospheric chemistry, calculation of J-values for shorter wavelengths, and improved modeling
127 of high-altitude aerosols. Extension of the chemistry mechanism to include reactions relevant to
128 the stratosphere enables the capturing of stratospheric responses and troposphere–stratosphere
129 coupling. UCX adds 28 species and 104 kinetic reactions, including 8 heterogeneous reactions,
130 along with 34 photolytic decompositions. Atomic oxygen [both $\text{O}({}^3\text{P})$ and $\text{O}({}^1\text{D})$] is explicitly
131 modeled; although also of short lifetime in the stratosphere, these species are important in correctly
132 modeling stratospheric chemistry. Photochemistry is extended up to the stratopause to high-energy
133 photons (177 nm) using the Fast-JX model, which includes cross-section data for many species
134 relevant to the troposphere and stratosphere. Photolysis rates respond to changes in the
135 stratospheric ozone layer. Additional heterogeneous reactions (Kirner et al., 2011, Rotman et al.,
136 2001, Shi et al., 2001) are included to capture seasonal ozone depletion. H_2O is treated as a
137 chemically-active advected tracer within the stratosphere. These permit chemical feedbacks
138 between stratospheric ozone and aerosols and tropospheric photochemistry. The improved GEOS-
139 Chem with coupled stratospheric–tropospheric responses has been evaluated with sonde and
140 satellite measurements of O_3 , HNO_3 , H_2O , HCl , ClO , NO_2 and stratospheric intrusions (Eastham
141 et al., 2014; Gronoff et al., 2021; Knowland et al., 2022). Yu and Luo (2009) incorporated a size-
142 resolved (sectional) APM package into GEOS-Chem, henceforth referred to as GC-APM. The
143 APM separates secondary particles from primary particles, uses 40 bins to represent secondary
144 particles with high size resolution for the size range important for the growth of nucleated particles
145 to accumulation mode sizes, and contains options to calculate nucleation rates based on different

146 nucleation schemes. In GEOS-Chem/APM, nucleation is calculated before condensation using a
147 time-splitting technique. Therefore, no competition between nucleation and condensation for
148 sulfuric acid vapor is considered. In most conditions, nucleation consumes only a very small
149 fraction (<1%) of sulfuric acid vapor in the air and the time splitting does not affect the results.
150 When nucleation rate is high, reduced time step for nucleation and growth is used to ensure that
151 the fraction of sulfuric acid vapor consumed by nucleation each time step is small. The GC-APM
152 uses a semi-implicit scheme to calculate sulfuric acid condensation together with sulfuric acid gas
153 phase production to ensure that the change of sulfuric acid vapor concentration is smooth. APM is
154 fully coupled with GEOS-Chem in both the troposphere and stratosphere, and is employed for the
155 present study.

156 In the present study we have carried out GEOS-Chem-UCX/APM global simulations from
157 01/2015 to 05/2018, with the first 17 months as spin-up and the remaining period covering ATom
158 1-4 periods (06/2016–05/2018). The horizontal resolution is $4^{\circ} \times 5^{\circ}$ and there are 72 vertical layers.
159 Emissions from different sources, regions, and species are computed via the Harvard-NASA
160 Emissions Component (HEMCO) on a user-defined grid (Keller et al., 2014). Historical global
161 anthropogenic emissions are based on the Community Emissions Data System (CEDS) inventory
162 (Hoesly et al., 2018). Regional anthropogenic emissions over the United States, Canada, Europe,
163 and East Asia are replaced by regional emission inventories of the National Emissions Inventory
164 (NEI, <https://www.epa.gov/air-emissions-inventories/2017-national-emissions-inventory-nei-data>), the Air Pollutant Emission Inventory (APEI, <https://www.canada.ca/en/environment-climate-change/services/pollutants/air-emissions-inventory-overview.html>), the Co-operative
165 Programme for Monitoring and Evaluation of the Long-range Transmission of Air Pollutants in
166 Europe (EMEP, <https://www.emep.int/index.html>), and the MIX Asian emission inventory (Li et
167 al., 2017), respectively. Monthly mean aircraft emissions are generated based on the Aviation
168 Emissions Inventory v2.0 (Stettler et al., 2011). The aircraft particle emissions include nucleation
169 mode sulfate particles (Emission index = $2 \times 10^{17} / \text{kg-fuel}$, mean diameter = 9 nm, based on Kärcher
170 et al., 2000), and black carbon and primary organic carbon (POC) particles. Global biomass
171 burning is taken from Global Fire Emissions Database version 4 (van der Werf et al., 2017). The
172 volcanic emissions of SO₂ are taken from AeroCom point-source data (Carn et al., 2015). Fixed
173 global surface boundary conditions are applied for N₂O, CFCs, HCFCs, halons, OCS and long-
174 lived organic chlorine species (Eastham et al., 2014).
175

176 2.2 Airborne ATom measurements of PNSD

177 Measurements are essential in advancing our understanding of stratospheric aerosol properties
178 and the fundamental processes governing these properties. NASA's Atmospheric Tomography
179 Mission (ATom; Wofsy et al., 2021; Thompson et al., 2022) is a multi-agency effort that provides
180 global in situ aircraft observations of the vertical structure of aerosols from near surface to ~12 km
181 altitude. PNSDs are measured using the NOAA Aerosol Microphysical Properties (AMP) package
182 (Brock et al., 2019) comprising nucleation-mode aerosol size spectrometer(s) (NMASS)
183 (Williamson et al. 2018), ultra-high-sensitivity aerosol spectrometer(s) (UHSAS) (Kupc et al.
184 2018), and a laser aerosol spectrometer (LAS) covering aerosol sizes from 3 nm to 4.5 μm . The
185 aerosol number abundance can be obtained by integrating the PNSD measurements.
186

189 **2.3 The CLOUD (Cosmics Leaving OUtdoor Droplets) measurements**

190 Laboratory measurements of nucleation rates as a function of key controlled parameters have
 191 been carried out in a 26.1 m³ stainless steel cylinder chamber at the European Organization for
 192 Nuclear Research (CERN), in the framework of the CLOUD experiment (Cosmics Leaving
 193 OUtdoor Droplets) (e.g., Kirkby et al., 2011; Kürten et al., 2016; Dunne et al., 2016). Some of
 194 these experiments were conducted at the temperature in the range of those in the stratosphere
 195 (Kirkby et al., 2011; Dunne et al., 2016) which are used in this study to evaluate nucleation
 196 schemes under stratospheric conditions.

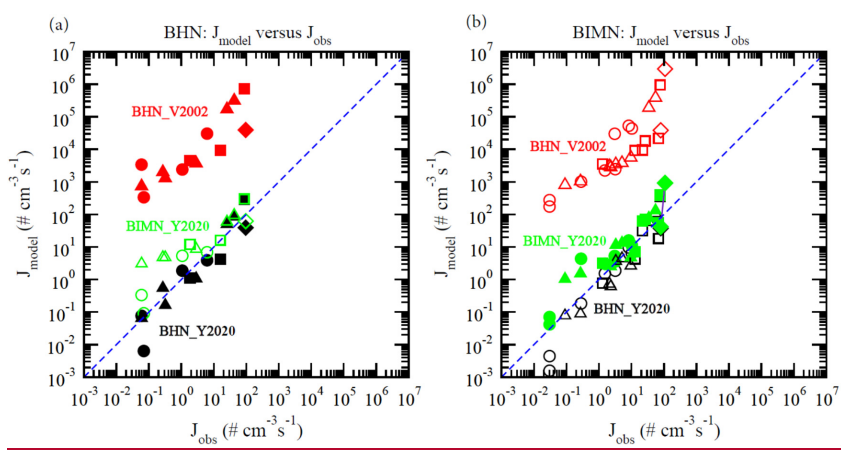
197

198 **3. Results**

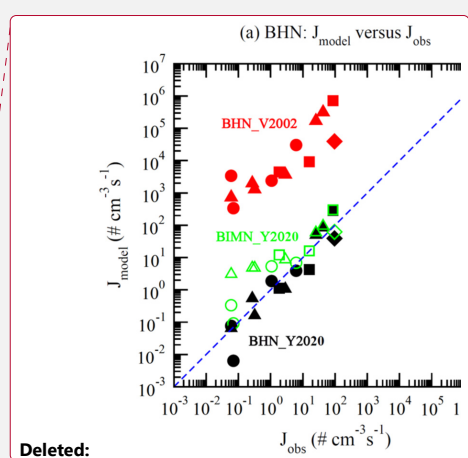
199 **3.1 H₂SO₄–H₂O binary homogeneous nucleation (BHN) and binary ion-mediated nucleation
 200 (BIMN) under stratospheric conditions**

201 Nucleation is one of the microphysical processes influencing particle size distributions in the
 202 stratosphere (Turco et al., 1982) The CLOUD measurements under a wide range of well-controlled
 203 conditions (Kirkby et al., 2011; Dunne et al., 2016) provide a unique set of data to evaluate the
 204 nucleation theories. Yu et al. (2020) compared nucleation rates calculated based on a number of
 205 commonly used aerosol nucleation parameterizations with the CLOUD measurements. Here we
 206 specifically examine the comparison under stratospheric conditions where temperature is below ~
 207 230 K. Since ammonia concentrations in the stratosphere are generally negligible, we focus on
 208 binary nucleation in the present study. The contribution of organics to particle formation, growth,
 209 and compositions in the upper troposphere and LMS has been investigated in several studies (Kupc
 210 et al., 2020; Murphy et al., 2021; Williamson et al., 2021). Because of the lack of information with
 211 regard to the low volatile gaseous organic species, the possible role of organics in new particle
 212 formation in LWS is not considered in the present study.

213



214 **Figure 1.** Comparison of nucleation rates based on three different schemes with CLOUD
 215 measurements within the low temperature range (T = 205–223 K) as that in the stratosphere for (a)
 216 binary homogeneous nucleation (no ionization) and (b) ion nucleation (at the presence of
 217 ionization rates 2.51 – 110 ion-pairs cm⁻³s⁻¹). The different nucleation schemes shown are: BHN
 218



220 of Vehkamäki et al. (2002) (BHN_V2002), BHN of Yu et al. (2020) (BHN_Y2020), and BIMN
221 of Yu et al. (2020) (BIMN_Y2020). For comparison, under binary condition of (a), BIMN rates at
222 $Q = 20$ ion-pairs $\text{cm}^{-3}\text{s}^{-1}$ are given while under binary ion nucleation condition of (b), BHN rates
223 are also given. Values of H_2SO_4 vapor concentration ($[\text{H}_2\text{SO}_4]$) range from 10^6 to $3 \times 10^7 \text{ cm}^{-3}$ and
224 are separated into four groups in the plots (Circles: $10^6 - 5 \times 10^6 \text{ cm}^{-3}$; triangles: $5 \times 10^6 - 10^7 \text{ cm}^{-3}$;
225 Squares: $10^7 - 1.5 \times 10^7 \text{ cm}^{-3}$; Diamonds: $1.5 \times 10^7 - 3 \times 10^7 \text{ cm}^{-3}$).

Deleted: $[\text{H}_2\text{SO}_4]$

Deleted: v

226
227 Figure 1 compares nucleation rates based on the following three different schemes with
228 CLOUD measurements under stratospheric temperature range ($T = 205-223 \text{ K}$): BHN of
229 Vehkamäki et al. (2002) (BHN_V2002), BHN of Yu et al. (2020) (BHN_Y2020), and BIMN of
230 Yu et al. (2020) (BIMN_Y2020). BHN_V2002 and BHN_Y2020 differ in term of thermodynamic
231 data and nucleation approach used (Yu et al., 2020). To show the relative importance of
232 homogeneous versus ion nucleation, BIMN rates at $Q = 20$ ion-pairs $\text{cm}^{-3}\text{s}^{-1}$ were given under
233 binary homogeneous condition in Fig. 1a and BHN rates were also given under binary ion
234 nucleation condition in Fig. 1b. Nucleation rates based on BHN_V2002 are consistently 3–5 orders
235 of magnitude higher than those observed under H_2SO_4 – H_2O binary nucleation conditions without
236 (Fig. 1a) and with (Fig. 1b) the effect of ionizations, while those based on BHN_Y2020 and
237 BIMN_Y2020 are close to the observed values. It should be noted that similar to the CLOUD
238 measurements with the effect of ionization, BHN rates are included in the BIMN rates (Yu et al.,
239 2018) and the difference between BIMN and BHN rates indicates the contribution of ion mediated
240 or induced nucleation. Under the conditions of Fig. 1a, assuming ionization rate of 20 ion-pairs
241 $\text{cm}^{-3}\text{s}^{-1}$ (within the range of its typical value in the stratosphere) the BIMN rates are about one
242 order of magnitude higher than BHN rates when the nucleation rates are below $\sim 5 \text{ cm}^{-3}\text{s}^{-1}$ but
243 close to BHN rates when nucleation rates are above $\sim 5 \text{ cm}^{-3}\text{s}^{-1}$. Similar difference between
244 BHN_Y2020 and BIMN_Y2020 can also be seen in Fig. 1b, indicating the importance of ion
245 nucleation at relatively lower nucleation rates (mostly associated with relatively lower $[\text{H}_2\text{SO}_4]$)
246 and dominance of homogeneous nucleation at higher nucleation rates (associated with larger
247 $[\text{H}_2\text{SO}_4]$). As we show next, $[\text{H}_2\text{SO}_4]$ in the background stratosphere is generally quite low and
248 thus ion nucleation dominates but BHN can become important in the SO_2 plumes injected into the
249 stratosphere.

Deleted: BHN and BIMN

Deleted: . The nucleation schemes shown are:

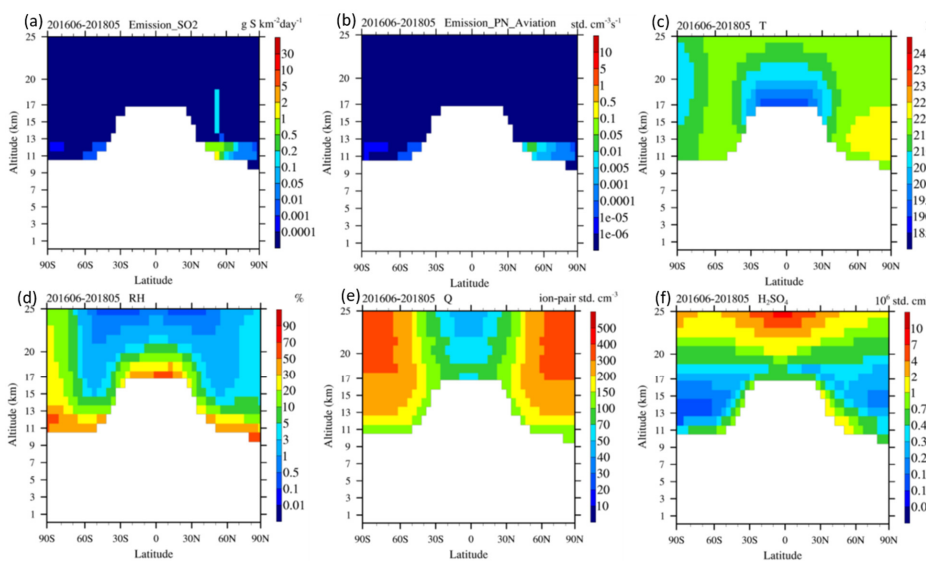
251 3.2 Nucleation rates and particle number concentrations in the stratosphere

252 Figure 2 shows the zonal mean SO_2 emission ($\text{SO}_2_{\text{emit}}$), particle number emitted by aviation
253 ($\text{PN}_{\text{aviation}}$), temperature (T), relative humidity (RH), ionization rate (Q), and $[\text{H}_2\text{SO}_4]$ averaged
254 during the two-year period (06/2016–05/2018) covering ATom 1-4. To focus on lower stratosphere
255 (LS), only the values of these variables in the stratosphere (grid boxes with more than 50% time
256 above tropopause) are shown. The SO_2 emissions include all sources including volcanos and
257 aviation. During this period, there was one relatively strong volcanic event, the Bezymianny
258 volcano (55.98°N, 160.59°E), on December 20, 2017 that injected $5 \times 10^6 \text{ kg S}$ into an altitude of \sim
259 14–18 km (Carn et al., 2015). Aviation emission is generally limited to below $\sim 12.5 \text{ km}$ altitude.
260 Based on MERRA2 meteorology data, which is used to drive GEOS-Chem, almost all of grid
261 boxes at 12 km are under the tropopause in the tropics (30°N–30°S), most of grid boxes at 12 km
262 in the high latitude regions (60°N–90°N, 60°S–90°S) are above tropopause, and some fractions of
263 grid boxes at 12 km in the middle latitude regions (30°N–60°N, 30°S–60°S) are above tropopause.

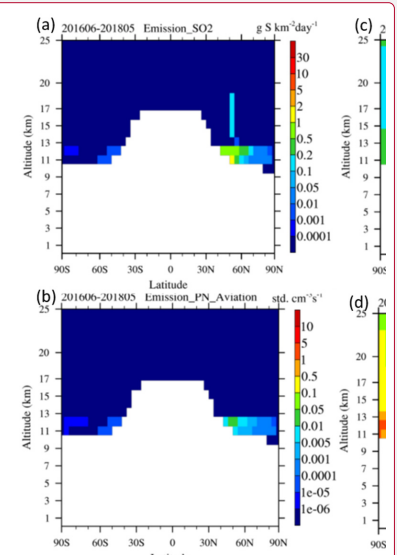
Deleted: SO_2

Deleted: at 52°N (Fig. 2a).

270 As can be seen from Fig. 2b, some of aviation emissions in the middle and high latitude regions
 271 are in the LMS, and the amount emitted into NH LMS is much higher (by several orders of
 272 magnitude) than that in SH. The temperature in the LS ranges from 190–225K, with the lowest
 273 value in the region just above tropical tropopause (Fig. 2c). RH in LS has highest values near
 274 tropopause but drops quickly with increasing altitude, from ~30–50% near tropopause to ~0.1–1%
 275 at ~ 25 km in the tropical and middle latitudes (Fig. 2d). The spatial variations of T and RH have
 276 important effects on nucleation in LS. The cosmic ray induced ionization rate in LS has large
 277 latitudinal gradient, ranging from ~40–100 ion-pair std. $\text{cm}^{-3}\text{s}^{-1}$ (here “std. cm^{-3} ” refers to per cubic
 278 centimeter at standard temperature and pressure, 273 K and 1013 hPa respectively) in the tropics
 279 to 100–400 ion-pair std. $\text{cm}^{-3}\text{s}^{-1}$ in middle and high latitude region (Fig. 2e). The high ionization
 280 rates may have important implication for particle microphysics in LS, which will also be discussed
 281 in Section 3.3. H_2SO_4 is the most important aerosol precursor in LS and its concentration depends
 282 on SO_2 concentrations and oxidation, condensation sink, and its vapor pressure that depends on T
 283 and RH. The annual mean $[\text{H}_2\text{SO}_4]$ (Fig. 2f) has large spatial variations, ranging from a minimum
 284 of $\sim 1\text{--}2 \times 10^5$ std. cm^{-3} at altitudes of $\sim 12\text{--}15$ km in polar regions to $\sim 4\text{--}20 \times 10^5$ std. cm^{-3} close
 285 to the tropopause. From $\sim 18\text{--}25$ km (well above the ATom measurement altitude), $[\text{H}_2\text{SO}_4]$
 286 increases with altitude, mainly due to the increasing H_2SO_4 vapor pressure associated with vertical
 287 changes of T (Fig. 2c) and RH (Fig. 2d).
 288
 289



290
 291 **Figure 2.** Zonal mean $\text{SO}_2_{\text{emit}}$, PN_{Emit} , T , RH , Q , and $[\text{H}_2\text{SO}_4]$ averaged during the two-year
 292 period (06/2016-05/2018) covering ATom 1-4. To focus on the lower stratosphere, only the values
 293 of these variables in grid boxes with more than 50% time above tropopause and below 25 km are
 294 shown.



Deleted:

296 To demonstrate the effect of nucleation schemes on simulated aerosol properties, we compare
297 in Fig. 3 zonal mean and vertical profiles of nucleation rates (J) and number concentrations of
298 condensation nuclei larger than 3 nm (CN3) simulated based on the three nucleation schemes:
299 BHN_V2002, BHN_Y2020, and BIMN_Y2020. In all three schemes, the aviation emissions of
300 both SO_2 (Fig. 2a) and particle numbers (Fig. 2b) are the same. The model simulations indicate
301 that NPF occurs in the lower stratosphere but is mostly confined to LMS except in the area of
302 volcano injection (for example, above ~ 14 km around $\sim 52^\circ\text{N}$). There exist large differences in
303 the nucleation rates predicted by the three schemes (noting the logarithmic color scale), with
304 BHN_V2002 rates generally 1–4 orders of magnitude higher while BIMN_Y2020 rates \sim one
305 order of magnitude higher than those based on BHN-Y2020. The difference between
306 BIMN_Y2020 and BHN_V2002 rates are smaller in the LMS over tropics (30°S–30°N) where
307 temperature is the lowest (see Fig. 2c). The magnitudes of differences are consistent with
308 comparisons with CLOUD measurements (Fig. 1). The difference in nucleation rates leads to
309 substantial difference in CN3 in LMS, with those based on BHN_V2002 a factor 2–5 higher than
310 those based on BHN_Y2020 in LMS. LMS CN3 based on BIMN_Y2020 is about 50% higher than
311 that of BHN_Y2020. Compared to the difference in nucleation rates, the differences in CN3 is
312 much smaller. This is expected because on one hand only a small fraction of nucleated particles
313 survive the coagulation scavenging and grow beyond 3 nm, and on the other hand direct emission
314 of particle numbers from aviation (Fig. 2b; treated as direct emission but most of these are actually
315 nucleated on chemi-ions in the exhaust plume shortly after emission) (Brock et al., 2000) and
316 transport provide substantial amount of CN3 even without nucleation. Nevertheless, nucleation is
317 still significant enough to affect the CN3. It is interesting to note that CN3 based on BIMN_Y2020
318 is higher at altitudes $> \sim 22$ km (Fig. 3h), which is associated with higher nucleation rates based
319 on BIMN_Y2020 than those based on BHN_V2002 and BHN_Y2020 within the altitude range of
320 35–55 km. Another interesting point is that there is a much smaller vertical gradient in
321 BHN_V2002 nucleation rates in the tropical region (30S–30N) within ~ 17 –20 km (see Figs. 3a
322 and 3d), likely a result of different dependences of nucleation rates based on different schemes on
323 T, RH, and $[\text{H}_2\text{SO}_4]$ which have large vertical variations (see Fig. 2). It can be seen from Fig. 3
324 that the simulations based on three nucleation schemes all show large hemispheric difference in
325 particle number concentrations (by a factor of \sim 3–6) in LMS at middle and high latitudes,
326 consistent with the ATom measurements (Williamson et al., 2021). Our sensitivity study (by
327 turning off aviation emission, not shown, to be reported in a separate study) indicates this large
328 hemispheric difference is largely caused by aviation emissions, confirming the analysis of
329 Williamson et al. (2021).
330

Deleted: S

334 **Figure 3.** Model simulated zonal mean and vertical profiles of nucleation rates (J; upper panels)

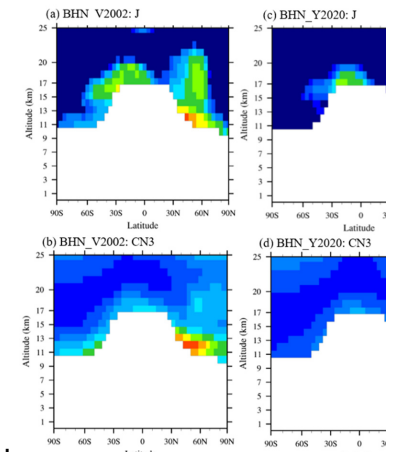
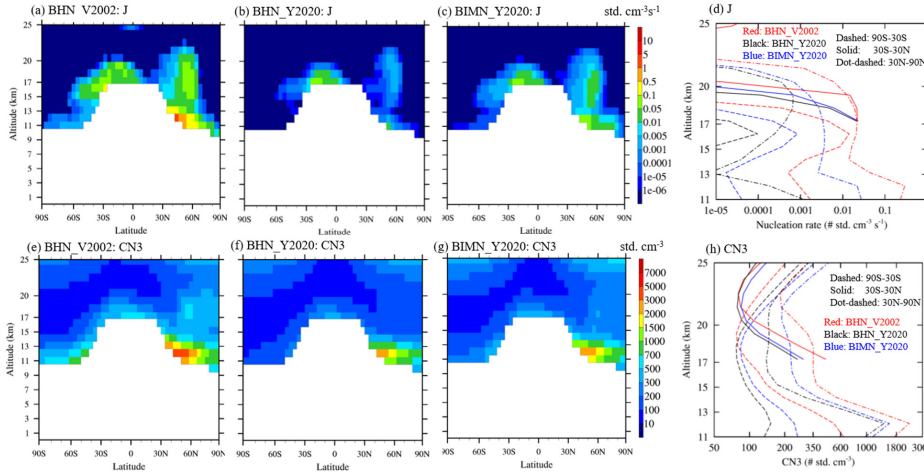
335 and number concentrations of particles larger than 3 nm (CN3; lower panels) in the stratosphere

336 during the two-year period covering ATom 1-4 (06/2016- 05/2018), based on three nucleation

337 schemes (a&e: BHN_V2002, b&f: BHN_Y2020, and c&g: BIMN_Y2020). The vertical profiles

338 for those grids with at least 50% of time above the tropopause are shown.

340 While it is difficult to observe nucleation rates in the stratosphere, the measurement of freshly
 341 nucleated nanoparticles can be used to constrain nucleation schemes. Figure 4a compares the
 342 model simulated CN3 (all particles with diameter larger than 3 nm, with the upper size limit of 12
 343 μm corresponding to the size of last model bin) based on the three nucleation schemes at altitudes
 344 of around 12 km in SH middle and high altitudes during four seasons with the corresponding ATom
 345 1-4 observations. As an example, Figures 4b-d show the model simulated horizontal distributions
 346 of CN3 at 12 km altitude during ATom 4 with the values and locations of ATom4 CN3 data
 347 overlaid. We choose SH for comparison, as it represents the background stratosphere with
 348 minimum influence of anthropogenic emissions (i.e., aviation) (Fig. 2b), to avoid the uncertainty
 349 associated with aviation emissions. In Figure 4, the model results are two-month average
 350 corresponding to the flight months of each ATom campaign while the measurement data points
 351 shown are those sampled within the altitudes range of 11.5-12.5 km, in the stratosphere
 352 (ozone>250 ppbv and RH<10%, following the same stratosphere definitions as in Murphy et al.
 353 (2021) and Williamson et al. (2021)), and averaged to a $4^\circ\text{x}5^\circ$ gridbox for comparison with
 354 modeled results. The impact of nucleation scheme on CN3 can be clearly seen: BHN_V2002
 355 overpredicted CN3 by a factor of 2-4, BHN_Y2020 slightly underpredicted CN3, and
 356 BIMN_Y2020 slightly overpredicted CN3. The larger vertical spread in CN3 from BHN_V2002
 357 is caused by the large CN3 latitude gradient associated with higher nucleation near tropopause



Deleted: a

Deleted: b

Deleted: c

Deleted: d

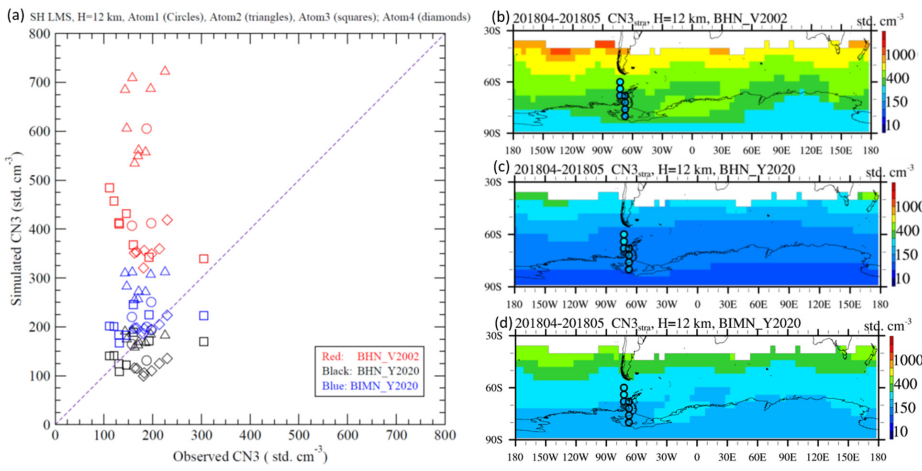
Deleted: e

Deleted: f

Deleted: g

Deleted: V

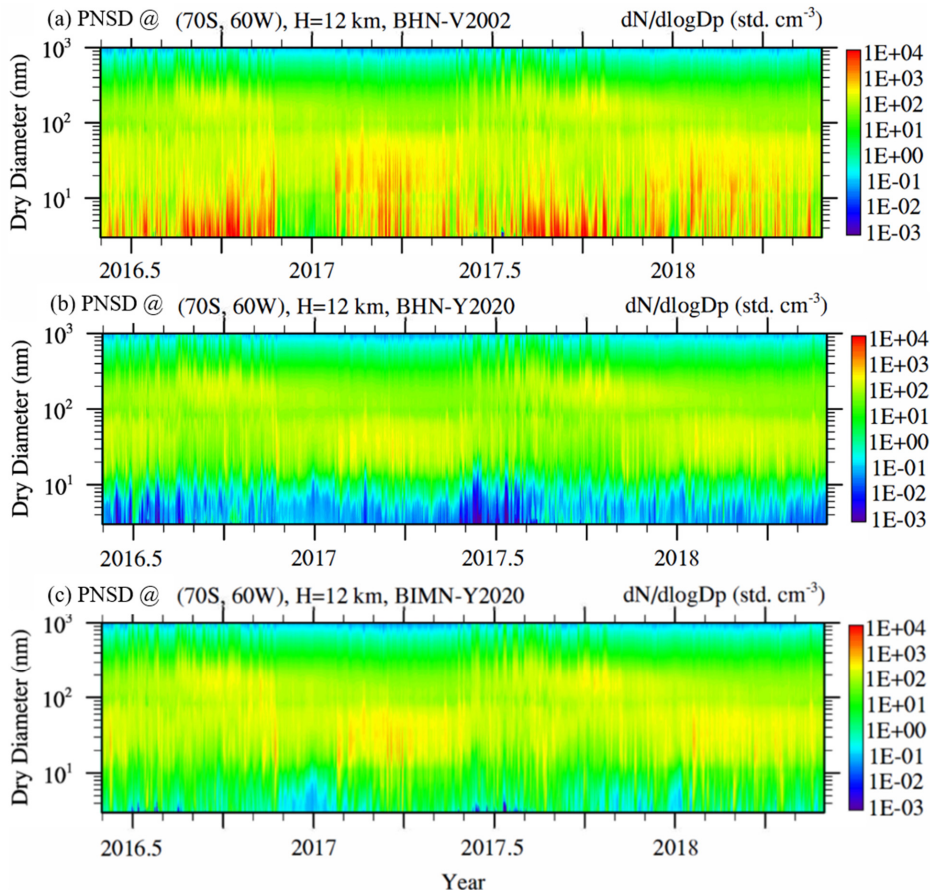
367 (Fig. 3). The comparisons above show that the ATom measurements provide a good constraint on
 368 our understanding of the processes controlling CN3 in the LMS at mid-high latitudes.
 369



370
 371 **Figure 4.** CN3 at altitudes of around 12 km in SH middle and high latitudes: (a) Model simulated
 372 versus observed during ATom 1-4 (Circles: ATom1; Triangles: ATom2; Squares: ATom3;
 373 Diamonds: ATom4); (b-d) model simulated horizontal distributions corresponding to ATom 4
 374 based on three different nucleation schemes (BHN_V2002, BHN_Y2020, and BIMN_Y2020),
 375 with the values and locations of ATom 4 CN3 measurements shown in the circles.

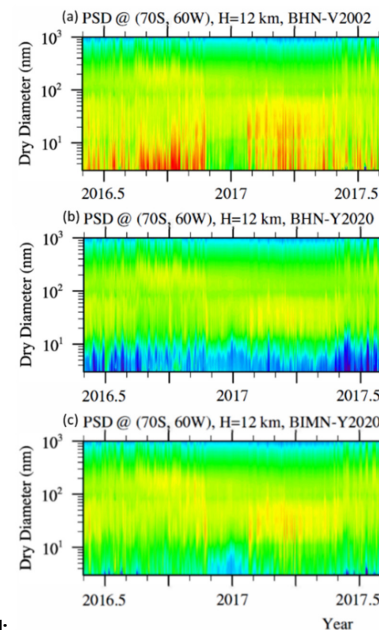
376 3.3 PNSDs in the stratosphere

377 Figure 5 shows the model simulated evolution of PNSDs at an altitude of 12 km over a site in
 378 SH (70°S, 60°W) during the two-year ATom period based on the three different nucleation
 379 schemes. The PNSDs shown in Fig. 5 are averaged into four different seasons corresponding to
 380 the months of ATom 1-4 field campaigns and are presented in Fig. 6 for comparison with the
 381 observed mean PNSDs in SH LMS (Williamsons et al., 2021). It should be noted that modeled
 382 PNSDs in Fig. 6 are two-month average at one fixed site at an altitude of 12 km (in the region
 383 where many of SH LMS measurements were taken, see Fig. 4) while the observed ones are
 384 averaged over all SH LMS air mass sampled during the corresponding ATom campaign. While
 385 the comparison in Fig. 6 is not exactly coterminous, it allows us to make quantitative comparisons
 386 of modeled and observed PNSDs. To take into account the variations in both model and observed
 387 PNSDs, standard deviations are shown as error bars in the measured and modeled curves based on
 388 BIMN_Y2020.
 389



391
392 **Figure 5.** Model simulated evolution of PNSDs at a site in SH (70S, 60 W) at altitude of 12 km
393 based on three nucleation schemes (BHN_2002, BHN_Y2020, and BIMN_Y2020).

394
395 Figure 6 shows that PNSDs measured in the background LMS have multiple modes: a
396 nucleation mode (NuclM: $\lesssim 10$ nm), an Aitken mode (AitkenM: $\sim 10 - 80$ nm), and two
397 accumulation modes (AccuM1: $\sim 80 - 250$ nm and AccuM2: $\sim 250 - 700$ nm). It should be noted
398 that these modes are not the same size limits as those presented in the public ATom dataset. As
399 shown in Figures 5 and 6, the model based on all three nucleation schemes generally captures the
400 AitkenM and AccuM1 and the existence of a minimum in PNSDs around 80 nm, although there
401 exist differences. Interestingly, the relative height (or peak values of $dN/dlogD_p$) of AitkenM and
402 AccuM1 has strong seasonal variations. The model captures a relatively higher AitkenM in SH
403 Summer and Fall and a higher AccuM1 in SH Spring. The model simulated PNSDs also agree

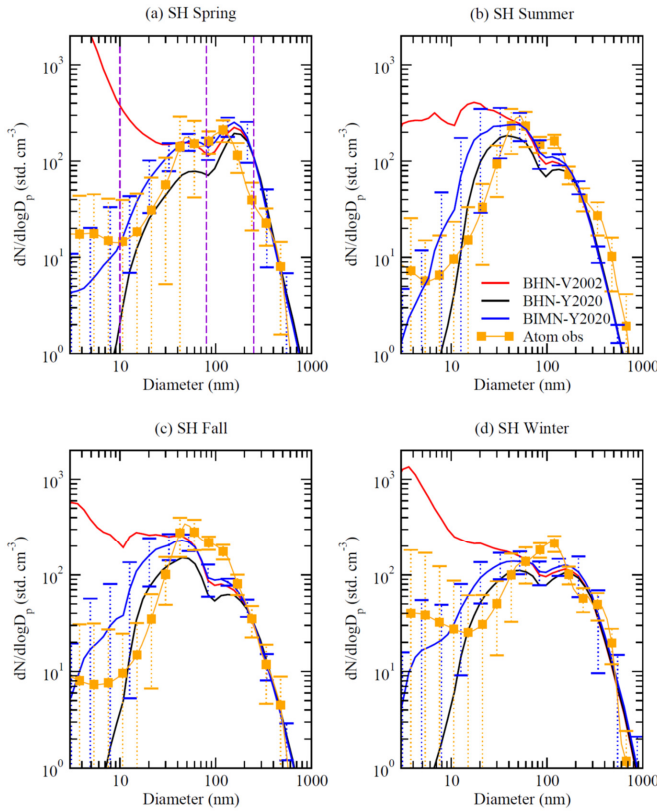


Deleted:

407 well with the measurements in term of the size-dependent normalized standard deviation (σ_{N} , i.e.,
408 the standard deviation σ divided by the mean); relatively smaller σ_{N} for Accum1 and larger size
409 part of AitkenM and much larger σ_{N} for NuclM, smaller size part of AitkenM, and Accum2. While
410 the larger σ_{N} for NuclM is understandable because of NPF, it is surprising for Accum2. The
411 Accum2 particles have relatively long lifetime and are expected to be well-mixed (and thus have
412 small variations) in LS. The transport of Accum2 particles from UT may contribute to the larger
413 variations. Murphy et al. (2021) showed the chemical signature of this transported mode, and here
414 we show that the variation in the size distribution may also contain information about the mixing
415 of UT particles into LMS. Compared to the observations, the model simulated Accum2 σ_{N} are
416 larger in SH Winter and Spring but are smaller in SH Summer and Fall. The possible reasons for
417 the large variations of Accum2 in LMS and the differences between model simulations and
418 measurements remain to be studied.

Deleted: s
Deleted: standard deviations
Deleted: standard deviations
Deleted: standard deviations

Deleted: standard deviation
Deleted: s



419
420 **Figure 6.** Model simulated seasonal mean PNSDs at a site in SH (70°S, 60°W) at altitude of 12
421 km based on three nucleation schemes and comparisons with the corresponding ATom
422 measurements (a: SH Spring 09–10/2017, b: SH Summer 01–02/2017, c: SH Fall 04–05/2018, and

429 d: SH Winter 06–07/2016). To take into account the variations in both model and observed PNSDs,
430 standard deviations are shown as error bars in the measured and modeled curves based on
431 BIMN_Y2020. Three vertical dashed lines at 10 nm, 80 nm, and 250 nm are drawn in (a) to guide
432 the eye to the four modes discussed in the text.

433
434

435 The large impacts of nucleation schemes on PNSDs, especially those smaller than 100 nm, can
436 be seen in Fig. 6. The formation rates and concentrations of nucleation mode particles are very
437 high based on BHN_V2002 (peak $dN/d\log D_p$ values reaching well above $10^3 \text{ std. cm}^{-3}$), negligible
438 based on BHN_Y2020 ($dN/d\log D_p$ values for particles $< 10 \text{ nm}$ are generally below 1 std. cm^{-3}),
439 and moderate based on BIMN_Y2020. When compared to the observed values, the number
440 concentrations of particles within 3–10 nm based on BHN_V2002 are 1–2 orders of magnitude
441 too high but those based on BHN_Y2020 are 1–2 orders of magnitudes too low, while those based
442 on BIMN_Y2020 are of the same order of magnitude. The impact of nucleation schemes on NuclM
443 propagates into the AitkenM and AccuM1, with BHN_Y2020 giving the lowest number
444 concentrations while BHN_V2002 gives the highest AitkenM and BIMN_Y2020 gives the highest
445 AccuM1. It should be noted that, while the line of BHN-Y2020 is lower than that of BIMN and
446 BHN-V2002 for particles of smaller sizes ($< 300 \text{ nm}$), it is slightly higher for larger particles ($> 300 \text{ nm}$).
447 This is consistent with the competition of sulfuric acid gas between pre-existing larger
448 particles and nucleated smaller particles. It is interesting to note that AccuM1 based on
449 BIMN_Y2020 is higher than that based on BHN_V2002 although BHN_V2002 predicts higher
450 NuclM and AitkenM, indicating a non-linear interaction among nucleation, growth, and
451 coagulation. The competition between nucleation and condensation for available sulfuric acid gas
452 has been shown to be important for SAI studies (Laakso et al., 2022).

453 There exist a number of differences in the simulated and observed PNSDs. Firstly,
454 measurements indicate a slight increase of $dN/d\log D_p$ with decreasing sizes for particles $< 10 \text{ nm}$
455 but the simulated PNSDs based on BIMN_Y2020, the scheme mostly consistent with CLOUD
456 measurements and predicting NuclM concentrations closest to those observed, decreases with
457 decreasing sizes for particles $< 10 \text{ nm}$. The possible reasons of the difference remain to be
458 investigated but probably are associated with uncertainty in nucleation rates and size-dependent
459 growth rates of freshly nucleated particles, and/or the fact that ATom observations are bias towards
460 daytime. In addition, the small number of particles in this mode is likely within the uncertainty in
461 the ATom measurements (about 7% of the total number of particles), so that this measured mode
462 may not be significant. Secondly, the model appears to overpredict the smaller size part (~ 10 – 40
463 nm) of AitkenM although it is close to the larger part (~ 40 – 80 nm). The overprediction
464 may be a result of the underestimated growth rates or coagulation scavenging rates of these
465 particles or overpredicted growth rates of NuclM particles. Thirdly, the model generally
466 overpredicts the mean mode sizes of AccuM1 and underpredicts the concentrations of the mode
467 except in SH Spring. The nucleation schemes have observable effects on the concentrations and
468 mean sizes of AccuM1 and overall the simulations based on BIMN_Y2020 are in stronger
469 agreement with measurements. Finally, the observed PNSDs show a clear AccuM2 in all seasons
470 except Fall but such a mode cannot be clearly seen in the model simulated PNSDs, indicating that
471 the model underpredicts the concentrations of AccuM2 mode particles. AccuM2 particles are

Deleted: the model does not predict the existence of the mode at all

474 within the size range with most efficient scattering of solar radiation and thus are important for
475 SAI. It is therefore necessary to identify the sources of this difference and to improve the model.

476 As pointed out earlier, the comparison in Fig. 6 does not exactly match in terms of time and
477 location, which likely contributes to some of the differences shown in Fig. 6. Some of the
478 differences can also be caused by the uncertainties in the model in term of emissions, transport,
479 chemistry, aerosol microphysics, and deposition. Nevertheless, some of these differences,
480 especially the shape of PNSDs (AccuM2, NuclM, etc.), are unlikely to be fully accounted for by
481 the above-mentioned possible mismatch or model uncertainties and thus may indicate that some
482 fundamental processes are not represented in the model. One possible cause of the differences is
483 that the transport of organic-sulfate particles from UT (Murphy et al., 2014, 2021) is not properly
484 simulated by the model. Based on size-resolved particle composition measurements, Murphy et al.
485 (2021) showed that the LMS accumulation mode particles (diameter ~ 0.1 and $1.0 \mu\text{m}$) have at
486 least two modes: the larger mode consists mostly of sulfuric acid particles produced in the
487 stratosphere, and the smaller mode consists mostly of organic-sulfate particles transported from
488 the troposphere. Murphy et al. (2014) showed that the fraction of organic-sulfate aerosols above
489 tropopause decreases quickly with altitudes. While the organic-sulfate mode aerosols from UT
490 may contribute to the bi-modal structure of accumulation mode particles in the LMS observed
491 during ATom, it is unlikely to contribute to the bi-modal structure of particles larger than $\sim 200 \text{ nm}$
492 observed at altitude above $\sim 20 \text{ km}$ both in the background and in volcano perturbed stratosphere
493 (Deshler et al., 2013, 2019; also see Fig. 7). Here, we suggest that the role of charges on
494 coagulation and growth of particles in the stratosphere could be another process causing the bi-
495 modal of large particles in the stratosphere.

496 As shown Fig. 2e, ionization rates are high in LS, ranging from ~ 40 – 100 ion-pair std. $\text{cm}^{-3}\text{s}^{-1}$.
497 Due to their low number concentrations (~ 100 – 1000 std. cm^{-3}) but long lifetime, particles in the
498 stratosphere are expected to be in charge equilibrium. Figure 7 shows mean particle number size
499 distribution (PNSD) and particle volume size distribution (PVSD) observed during ATom 1-4 in
500 SH LMS and measured within 20–25 km altitude over Lararie WY in 1992, and fraction of particles
501 carrying n charges based on the modified Boltzmann equilibrium equation (Clement and Harrison,
502 1992). The bi-modal structure of accumulation mode particles can be clearly seen in both
503 background and volcano perturbed stratosphere. It should be noted that while the smaller mode
504 generally dominates the number concentrations, the larger mode dominates mass concentrations.
505 Under equilibrium more particles are charged (i.e., $1-f_0 > 50\%$) than neutral (f_0) for particles with
506 diameter larger than $\sim 80 \text{ nm}$ and a significant fraction ($> 25\%$) of particles larger than 300 nm
507 carrying multiple charges. While the equilibrium charge fraction is small for NuclM particles (\lesssim
508 10 nm), this fraction can be much larger when nucleation on ions occurs, which is consistent with
509 the observed overcharging of freshly nucleated particles (Laakso et al. 2007; Yu and Turco, 2008).
510 Particle coagulation rates are influenced by forces exerted between colliding particles, including
511 van der Waals and electrostatic forces, which can modify the effective collision cross section and
512 sticking coefficient. The van der Waals force has been shown to be important in the stratosphere
513 (English et al., 2011, 2012) and has been considered in the simulations shown above. The effects
514 of charges on coagulation and implications for PNSDs in the stratosphere have not yet been studied
515 (to our knowledge). Since coagulation is a dominant process for the growth of accumulation mode
516 particles in the stratosphere, we hypothesize that differential coagulation rates for neutral and

Deleted: e

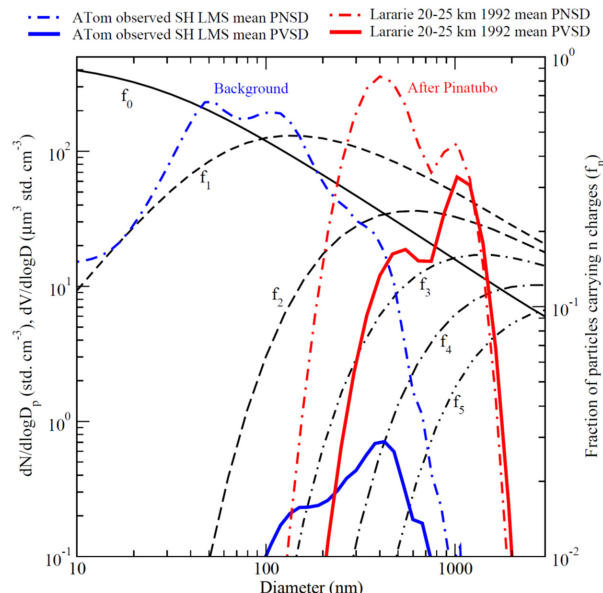
Deleted: e

Deleted: e

Deleted: e

521 charged particles in accumulation modes can potentially act as a physical process separating the
 522 modeled single accumulation mode (Fig. 6) into two modes (Accum1 and Accum2) as observed.
 523 Further research is needed to test this hypothesis. In addition to affecting coagulation, charge on
 524 small particles can also enhance the growth rate due to ion-dipole interactions of condensing
 525 molecules with charged particles (Nadykto and Yu, 2005). This enhancement is expected to be
 526 stronger in the stratosphere because of lower temperature (Nadykto and Yu, 2005). Beside these,
 527 Svensmark et al. (2020) showed that the condensation of ion clusters can enhance particle growth
 528 rates. How much the enhanced coagulation and growth rates of charged particles may shape
 529 PNSDs and modes in the stratosphere remains to be investigated.

530



531
 532 **Figure 7.** ATom 1-4 mean observed particle number size distribution (PNSD, or $dN/d\log D$) and
 533 particle volume size distribution (PVSD, or $dV/d\log D$) in SH LMS, balloon-borne measured
 534 mean PNSD and PVSD within 20-25 km altitude over Lararie WY in 1992, and fraction of
 535 particles carrying n ($n = 0, 1, 2, 3, 4$, and 5) charges based on the modified Boltzmann equilibrium
 536 equation (Clement and Harrison, 1992). Note that f_n with $n \geq 1$ including both positive and negative
 537 charges, i.e., for example, half of f_1 carrying one negative charge while the other half positive.

538

539 4. Summary and Discussions

540 Interest in stratospheric aerosols has been increasing in recent years, due to the ongoing
 541 discussion about the plausibility, potential benefits and risks of offsetting climate change through
 542 stratospheric aerosol injection (SAI) to buy time for reduction of CO_2 in the atmosphere. Recent
 543 studies indicate the dependence of SAI radiative efficacy (Dai et al., 2018) on the particle size
 544 distribution (NASEM, 2021) and thus it is critical to improve foundational understanding and

Deleted: efficiency

546 model representation of aerosol microphysics processes controlling the evolution of stratospheric
547 aerosols, both under background conditions and perturbed scenarios. While formation and growth
548 of particles in the troposphere have been extensively studied in the past two decades, very limited
549 efforts have been devoted to understanding these in the stratosphere.

550 In the present study we use both CLOUD laboratory measurements taken under very low
551 stratospheric temperatures and ATom in-situ observations of particle number size distributions
552 (PNSD) down to 3 nm to constrain nucleation schemes and model-simulated particle size
553 distributions in the lowermost stratosphere (LMS). We show that the binary homogenous
554 nucleation scheme used in most of the existing SAI modeling studies overpredicts the nucleation
555 rates by 3–4 orders of magnitude (when compared to CLOUD data), leading to significant
556 overprediction of particle number concentrations in the background stratosphere (by a factor of 2–
557 4 in SH LMS, compared to ATom data). Based on a recently developed kinetic nucleation model
558 which provides rates of both ion-mediated nucleation (IMN) and BHN at low temperatures in good
559 agreement with CLOUD measurements, both BHN and IMN occur in the stratosphere but IMN
560 rates are generally more than one order of magnitude higher than BHN rates and thus dominate
561 nucleation in the background stratosphere.

562 In the SH LMS that has minimal influences from anthropogenic emissions, our analysis shows
563 that ATom-measured PNSDs generally have four apparent modes: a nucleation mode (NuclM: \lesssim
564 10 nm), which may not be statistically significant, an Aitken mode (AitkenM: \sim 10–80 nm), and
565 two accumulation modes (AccuM1: \sim 80–250 nm and AccuM2: \sim 250–700 nm). The model
566 generally captures the AitkenM and AccuM1 and the existence of a minimum in PNSDs at \sim 80
567 nm, although there are differences. The model captures a relatively higher AitkenM in SH Summer
568 and Fall and a higher AccuM1 in SH Spring. The model simulated PNSDs also agree well with
569 the measurements in term of the size-dependent standard deviations: relatively smaller standard
570 deviations for AccuM1 and larger size part of AitkenM and much larger standard deviations for
571 NuclM, smaller size part of AitkenM, and AccuM2.

572 A detailed comparison indicates the existence of a third PNSD mode peaking around 300–400
573 nm in the ATom measurements that are not captured by the model. Compared to the observations,
574 the model-simulated AccuM2 standard deviations are larger in SH Winter and Spring but are
575 smaller in SH Summer and Fall. In addition, the model overpredicts the number concentration of
576 particles in the size range of 10–50 nm. These differences may indicate that, in addition to
577 nucleation, the model may be missing some fundamental microphysical processes of stratospheric
578 aerosols. Our analysis shows that, in the stratosphere, more particles are charged (positive +
579 negative) than neutral for particles with diameter larger than \sim 80 nm and a significant fraction ($>$
580 25%) of particles larger than 300 nm carrying multiple charges. We propose that the role of charges
581 on coagulation and growth of particles in the stratosphere, where ionization rates are high and
582 particles have very long lifetime, is likely one of such processes. Considering the importance of
583 accurate particle size distributions (especially the accumulation mode particles) for projecting
584 realistic radiative forcing response to stratospheric aerosols, it is essential to understand and
585 incorporate such potentially important processes in model simulations of future changes in the
586 stratosphere. It should be noted that the ATom measurement period does not have a high
587 stratospheric aerosol loading (i.e., no major volcano eruptions). It remains to be investigated if
588 previous assessments of volcanic aerosol microphysics missed something important. We expect

589 the uncertainties in the nucleation schemes and unknown cause of the bi-modal structure of
590 accumulation mode particles will affect particle optical properties and surface area and thus
591 radiative forcing or chemistry. The present work highlights the importance of advancing scientific
592 understanding of processes controlling properties of stratospheric particles as well as further
593 development, improvement, and validation of models for reducing uncertainties of SAI
594 simulations (e.g., Golja et al., 2021, Sun et al., 2022).

595 **Conflict of interest:** The authors declare that they have no conflict of interest.

596 **Acknowledgments.** The MERRA-2 data used in this study have been provided by the Global
597 Modeling and Assimilation Office (GMAO) at NASA Goddard Space Flight Center. This research
598 has been supported by NASA (grant nos. 80NSSC19K1275 and 80NSSC21K1199) and
599 SilverLining.

600 **Data availability.** The GEOS-Chem model is available to the public at <https://geos-chem.seas.harvard.edu/>. Simulation output in this analysis is available at
601 <https://doi.org/10.5281/zenodo.6909944>. The ATom dataset is published as Wofsy et al., (2021,
602 <https://doi.org/10.3334/ORNLDAAC/1925>) and is also available at
603 <https://espoarchive.nasa.gov/archive/browse/atom> (last access: June 2022).

604 **References**

605 Brock, C. A., Hamill, P., Wilson, J. C., Jonsson, H. H., and Chan, K. R.: Particle formation in the
606 upper tropical troposphere – A source of nuclei for the stratospheric aerosol, *Science*, 270,
607 1650–1653, <https://doi.org/10.1126/science.270.5242.1650>, 1995.

608 Brock, C. A., Schröder, F., Kärcher, B., Petzold, A., Busen, R., and Fiebig, M.: Ultrafine particle
609 size distributions measured in aircraft exhaust plumes, *J. Geophys. Res.-Atmos.*, 105, 26555–
610 26567, <https://doi.org/10.1029/2000jd900360>, 2000.

611 Brock, C. A., Williamson, C., Kupc, A., Froyd, K. D., Erdesz, F., Wagner, N., Richardson, M.,
612 Schwarz, J. P., Gao, R.-S., Katich, J. M., Campuzano-Jost, P., Nault, B. A., Schroder, J. C.,
613 Jimenez, J. L., Weinzierl, B., Dollner, M., Bui, T., and Murphy, D. M.: Aerosol size
614 distributions during the Atmospheric Tomography Mission (ATom): methods, uncertainties,
615 and data products, *Atmos. Meas. Tech.*, 12, 3081–3099, <https://doi.org/10.5194/amt-12-3081-2019>, 2019.

616 Brock, C.A., Froyd, K.D., Dollner, M., Williamson, C.J., Schill, G., Murphy, D.M., Wagner, N.J.,
617 Kupc, A., Jimenez, J.L., Campuzano-Jost, P., Nault, B.A., Schroder, J.C., Day, D.A., Price,
618 D.J., Weinzierl, B., Schwarz, J.P., Katich, J.M., Wang, S., Zeng, L., Weber, R., Dibb, J.,
619 Scheuer, E., Diskin, G.S., DiGangi, J.P., Bui, T., Dean-Day, J.M., Thompson, C.R., Peischl,
620 J., Ryerson, T.B., Bourgeois, I., Daube, B.C., Commane, R., and Wofsy, S.C. Ambient
621 aerosol properties in the remote atmosphere from global-scale in situ measurements, *Atmos.
622 Chem. Phys.*, 21: 15023-63. 2021.

623 Carn, S. A., Yang, K., Prata, A. J. and Krotkov, N. A.: Extending the long-term record of volcanic
624 SO₂ emissions with the Ozone Mapping and Profiler Suite nadir mapper. *Geophys. Res. Lett.*,
625 42: 925– 932. doi: 10.1002/2014GL062437, 2015.

630 [Clement, C. F., & Harrison, R. G.: The charging of radioactive aerosols. *Journal of Aerosol Science*, 23\(5\), 481–504. \[https://doi.org/10.1016/0021-8502\\(92\\)90019-R\]\(https://doi.org/10.1016/0021-8502\(92\)90019-R\), 1992.](https://doi.org/10.1016/0021-8502(92)90019-R)

631 [Dai, Z., Weisenstein, D. K., & Keith, D. W.: Tailoring meridional and seasonal radiative forcing by sulfate aerosol solar geoengineering. *Geophysical Research Letters*, 45, 1030–1039. <https://doi.org/10.1002/2017GL076472>, 2018.](https://doi.org/10.1002/2017GL076472)

632 [Dawson, M. L., Varner, M. E., Perraud, V., Ezell, M. J., Gerber, R. B., & Finlayson-Pitts, B. J.: Simplified mechanism for new particle formation from methanesulfonic acid, amines, and water via experiments and ab initio calculations. *Proceedings of the National Academy of Sciences*, 109\(46\), 18719–18724, 2012.](https://doi.org/10.1073/pnas.1220442109)

633 [Dunne, E. M., Gordon, H., Kürten, A., Almeida, J., Duplissy, J., Williamson, C., Ortega, I. K., Pringle, K. J., Adamov, A., Baltensperger, U., Barmet, P., Benduhn, F., Bianchi, F., Breitenlechner, M., Clarke, A., Curtius, J., Dommen, J., Donahue, N. M., Ehrhart, S., Flagan, R. C., Franchin, A., Guida, R., Hakala, J., Hansel, A., Heinritzi, M., Jokinen, T., Kangasluoma, J., Kirkby, J., Kulmala, M., Kupc, A., Lawler, M. J., Lehtipalo, K., Makhmutov, V., Mann, G., Mathot, S., Merikanto, J., Miettinen, P., Nenes, A., Onnela, A., Rap, A., Reddington, C. L. S., Riccobono, F., Richards, N. A. D., Rissanen, M. P., Rondo, L., Sarnela, N., Schobesberger, S., Sengupta, K., Simon, M., Sipilä, M., Smith, J. N., Stozkhov, Y., Tomé, A., Tröstl, J., Wagner, P. E., Wimmer, D., Winkler, P. M., Worsnop, D. R., and Carslaw, K. S.: Global particle formation from CERN CLOUD measurements, *Science*, 354, 1119–1124, <https://doi.org/10.1126/science.aaf2649>, 2016.](https://doi.org/10.1126/science.aaf2649)

634 [Eastham, S. D., Weisenstein, D. K., & Barrett, S. R.: Development and evaluation of the unified tropospheric–stratospheric chemistry extension \(UCX\) for the global chemistry-transport model GEOS-Chem. *Atmospheric Environment*, 89, 52–63, 2014.](https://doi.org/10.1016/j.atmosenv.2014.01.030)

635 [English, J. M., Toon, O. B., Mills, M. J., & Yu, F.: Microphysical simulations of new particle formation in the upper troposphere and lower stratosphere. *Atmospheric Chemistry and Physics*, 11\(17\), 9303–9322, 2011.](https://doi.org/10.1016/j.atmosenv.2011.05.030)

636 [Evans, M. J., & Jacob, D. J.: Impact of new laboratory studies of N₂O₅ hydrolysis on global model budgets of tropospheric nitrogen oxides, ozone, and OH. *Geophysical Research Letters*, 32\(9\), 2005.](https://doi.org/10.1029/2004GL019700)

637 [Golja, C. M., Chew, L. W., Dykema, J. A., & Keith, D. W.: Aerosol dynamics in the near field of the SCoPEx stratospheric balloon experiment. *Journal of Geophysical Research: Atmospheres*, 126, e2020JD033438. <https://doi.org/10.1029/2020JD033438>, 2021.](https://doi.org/10.1029/2020JD033438)

638 [Gronoff, G., Berkoff, T., Knowland, K. E., Lei, L., Shook, M., Fabbri, B., Carrion, W., & Langford, A. O.: Case study of stratospheric intrusion above Hampton, Virginia: lidar-observation and modeling analysis. *Atmospheric Environment*, 118498, 2021.](https://doi.org/10.1016/j.atmosenv.2021.118498)

639 [Hamill, P., Turco, R. P., Kiang, C. S., Toon, O. B., and Whitten, R. C.: An analysis of various nucleation mechanisms for sulfate particles in the stratosphere, *J. Aerosol Sci.*, 13, 561–585, 1982.](https://doi.org/10.1016/j.jaerosci.1982.00013)

640 [Hoesly, R. M., Smith, S. J., Feng, L., Klimont, Z., Janssens-Maenhout, G., Pitkanen, T., Seibert, J. J., Vu, L., Andres, R. J., Bolt, R. M., Bond, T. C., Dawidowski, L., Kholod, N., Kurokawa, J.-I., Li, M., Liu, L., Lu, Z., Moura, M. C. P., O'Rourke, P. R., and Zhang, Q.: Historical \(1750–2014\) anthropogenic emissions of reactive gases and aerosols from the Community Emissions Data System \(CEDS\), *Geosci. Model Dev.*, 11, 369–408, 2018.](https://doi.org/10.1029/2018CD015024)

673 Holmes, C. D., Bertram, T. H., Confer, K. L., Graham, K. A., Ronan, A. C., Wirks, C. K., & Shah,
674 V.: The role of clouds in the tropospheric NO_x cycle: A new modeling approach for cloud
675 chemistry and its global implications. *Geophysical Research Letters*, 46(9), 4980-4990, 2019.

676 IPCC. Climate Change 2021: The Physical Science Basis. Contribution of Working Group I to the
677 Sixth Assessment Report of the Intergovernmental Panel on Climate Change [Masson-
678 Delmotte, V., P. Zhai, A. Pirani, S. L. Connors, C. Péan, S. Berger, N. Caud, Y. Chen, L.
679 Goldfarb, M. I. Gomis, M. Huang, K. Leitzell, E. Lonnoy, J. B. R. Matthews, T. K. Maycock,
680 T. Waterfield, O. Yelekçi, R. Yu and B. Zhou (eds.)]. Cambridge University Press, 2021.

681 Jones, A., Haywood, J. M., Jones, A. C., Tilmes, S., Kravitz, B., and Robock, A.: North Atlantic
682 Oscillation response in GeoMIP experiments G6solar and G6sulfur: why detailed modelling
683 is needed for understanding regional implications of solar radiation management. *Atmos.*
684 *Chem. Phys.*, 21, 1287–1304, <https://doi.org/10.5194/acp-21-1287-2021>, 2021.

685 Kärcher, B., Turco, R. P., Yu, F., Danilin, M. Y., Weisenstein, D. K., Miake-Lye, R. C., & Busen,
686 R.: A unified model for ultrafine aircraft particle emissions. *Journal of Geophysical Research: Atmospheres*, 105(D24), 29379-29386, 2000.

687 Keller, C. A., Long, M. S., Yantosca, R. M., Da Silva, A. M., Pawson, S., and Jacob D. J.: HEMCO
688 v1.0: a versatile, ESMF-compliant component for calculating emissions in atmospheric
689 models, *Geosci. Model Dev.*, 7, 1409–1417, 2014.

690 Kerminen, V. M., Chen, X., Vakkari, V., Petäjä, T., Kulmala, M., & Bianchi, F.: Atmospheric new
691 particle formation and growth: review of field observations. *Environmental Research Letters*,
692 13(10), 103003, 2018.

693 Kirkby, J., Curtius, J., Almeida, J., Dunne, E., Duplissy, J., Ehrhart, S., Franchin, A., Gagné, S.,
694 Ickes, L., Kürten, A., Kupc, A., Metzger, A., Riccobono, F., Rondo, L., Schobesberger, S.,
695 Tsagkogeorgas, G., Wimmer, D., Amorim, A., Bianchi, F., Breitenlechner, M., David, A.,
696 Dommen, J., Downard, A., Ehn, M., Flagan, R. C., Haider, S., Hansel, A., Hauser, D., Jud, W.,
697 Junninen, H., Kreissl, F., Kvashin, A., Laaksonen, A., Lehtipalo, K., Lima, J., Lovejoy, E. R.,
698 Makhmutov, V., Mathot, S., Mikkilä, J., Minginette, P., Mogo, S., Nieminen, T., Onnela, A.,
699 Pereira, P., Petäjä, T., Schnitzhofer, R., Seinfeld, J. H., Sipilä, M., Stozhkov, Y., Stratmann,
700 F., Tomé, A., Vanhanen, J., Viisanen, Y., Vrtala, A., Wagner, P. E., Walther, H., Weingartner,
701 E., Wex, H., Winkler, P. M., Carslaw, K. S., Worsnop, D. R., Baltensperger, U., and Kulmala,
702 M.: The role of sulfuric acid, ammonia and galactic cosmic rays in atmospheric aerosol
703 nucleation, *Nature*, 476, 429–433, 2011.

704 Kirner, O., Ruhnke, R., Buchholz-Dietsch, J., Jöckel, P., Brühl, C., & Steil, B.: Simulation of polar
705 stratospheric clouds in the chemistry-climate-model EMAC via the submodel
706 PSC. *Geoscientific Model Development*, 4(1), 169-182, 2011.

707 Knowland, K. E., Keller, C. A., Wales, P. A., Wargan, K., Coy, L., Johnson, M. S., et al. (2022).
708 NASA GEOS Composition Forecast Modeling System GEOS-CF v1.0: Stratospheric
709 composition. *Journal of Advances in Modeling Earth Systems*, 14, e2021MS002852.
710 <https://doi.org/10.1029/2021MS002852>.

711 Kravitz, B., Robock, A., Boucher, O., Schmidt, H., Taylor, K. E., Stenchikov, G., & Schulz, M.:
712 The geoengineering model intercomparison project (GeoMIP). *Atmospheric Science*
713 Letters

714 12(2), 162-167, 2011.

715 Kulmala, M., Vehkamäki, H., Petäjä, T., Dal Maso, M., Lauri, A., Kerminen, V. M., W. Birmili,
716 & McMurry, P. H.: Formation and growth rates of ultrafine atmospheric particles: a review
717 of observations. *Journal of Aerosol Science*, 35(2), 143-176. doi:
718 10.1016/j.jaerosci.2003.10.003, 2004.

719 Kupc, A., Williamson, C., Wagner, N. L., Richardson, M., & Brock, C. A.: Modification,
720 calibration, and performance of the Ultra-High Sensitivity Aerosol Spectrometer for particle
721 size distribution and volatility measurements during the Atmospheric Tomography Mission
722 (ATom) airborne campaign. *Atmospheric Measurement Techniques*, 11(1), 369-383.
723 doi:10.5194/amt-11-369-2018, 2018.

724 Kupc, A., Williamson, C. J., Hodshire, A. L., Kazil, J., Ray, E., Bui, T. P., Dollner, M., Froyd, K.
725 D., McKain, K., Rollins, A., Schill, G. P., Thames, A., Weinzierl, B. B., Pierce, J. R., and
726 Brock, C. A.: The potential role of organics in new particle formation and initial growth in
727 the remote tropical upper troposphere, *Atmos. Chem. Phys.*, 20, 15037-15060, 10.5194/acp-
728 20-15037-2020, 2020.

729 Kürten, A., Bianchi, F., Almeida, J., Kupiainen-Määttä, O., Dunne, E. M., Duplissy, J., Williamson,
730 C., Barnet, P., Breitenlechner, M., Dommen, J., Donahue, N. M., Flagan, R. C., Franchin,
731 A., Gordon, H., Hakala, J., Hansel, A., Heinritzi, M., Ickes, L., Jokinen, T., Kangasluoma, J.,
732 Kim, J., Kirkby, J., Kupc, A., Lehtipalo, K., Leiminger, M., Makhmutov, V., Onnela, A.,
733 Ortega, I. K., Petäjä, T., Praplan, A. P., Riccobono, F., Rissanen, M. P., Rondo, L.,
734 Schnitzhofer, R., Schobesberger, S., Smith, J. N., Steiner, G., Stozhkov, Y., Tomé, A., Tröstl,
735 J., Tsagkogeorgas, G., Wagner, P. E., Wimmer, D., Ye, P., Baltensperger, U., Carslaw, K.,
736 Kulmala, M., and Curtius, J.: Experimental particle formation rates spanning tropospheric
737 sulfuric acid and ammonia abundances, ion production rates, and temperatures, *J. Geophys.
738 Res.-Atmos.*, 121, 12377–12400, <https://doi.org/10.1002/2015JD023908>, 2016.

739 Laakso, A., Niemeier, U., Visioni, D., Tilmes, S., and Kokkola, H.: Dependency of the impacts of
740 geoengineering on the stratospheric sulfur injection strategy – Part 1: Intercomparison of
741 modal and sectional aerosol modules, *Atmos. Chem. Phys.*, 22, 93–118,
742 <https://doi.org/10.5194/acp-22-93-2022>, 2022.

743 Laakso, L., Gagné, S., Petäjä, T., Hirsikko, A., Aalto, P. P., Kulmala, M., & Kerminen, V. M.:
744 Detecting charging state of ultra-fine particles: instrumental development and ambient
745 measurements. *Atmospheric Chemistry and Physics*, 7(5), 1333-1345, 2007.

746 Lee, S. H., Gordon, H., Yu, H., Lehtipalo, K., Haley, R., Li, Y., & Zhang, R.: New particle
747 formation in the atmosphere: From molecular clusters to global climate. *Journal of
748 Geophysical Research: Atmospheres*, 124(13), 7098-7146, 2019.

749 Lee, S. H., Reeves, J. M., Wilson, J. C., Hunton, D. E., Viggiano, A. A., Miller, T. M., Ballenthin,
750 J. O., and Lait, L. R.: Particle formation by ion nucleation in the upper troposphere and lower
751 stratosphere, *Science*, 301, 1886–1889, <https://doi.org/10.1126/science.1087236>, 2003.

752 Li, M., Zhang, Q., Kurokawa, J.-I., Woo, J.-H., He, K., Lu, Z., Ohara, T., Song, Y., Streets, D. G.,
753 Carmichael, G. R., Cheng, Y., Hong, C., Huo, H., Jiang, X., Kang, S., Liu, F., Su, H., and
754 Zheng, B.: MIX: a mosaic Asian anthropogenic emission inventory under the international
755 collaboration framework of the MICS-Asia and HTAP, *Atmos. Chem. Phys.*, 17, 935–963,
756 <https://doi.org/10.5194/acp-17-935-2017>, 2017.

757 Lockley, A., MacMartin, D., & Hunt, H.: An update on engineering issues concerning stratospheric
758 aerosol injection for geoengineering. *Environmental Research Communications*, 2(8),
759 082001, 2020.

760 Lovejoy, E. R., Curtius, J., and Froyd, K. D.: Atmospheric ion-induced nucleation of sulfuric acid
761 and water, *J. Geophys. Res.*, 109, D08204, <https://doi.org/10.1029/2003JD004460>, 2004.

762 Luo, G., Yu, F., & Moch, J. M.: Further improvement of wet process treatments in GEOS-Chem
763 v12. 6.0: impact on global distributions of aerosols and aerosol precursors. *Geoscientific
764 Model Development*, 13(6), 2879-2903, 2020.

765 Martin, R. V., Jacob, D. J., Chance, K., Kurosu, T. P., Palmer, P. I., & Evans, M. J.: Global
766 inventory of nitrogen oxide emissions constrained by space-based observations of NO₂
767 columns. *Journal of Geophysical Research: Atmospheres*, 108(D17), 2003.

768 Mills, M. J., Richter, J. H., Tilmes, S., Kravitz, B., MacMartin, D. G., Glanville, A. A., Tribbia, J.
769 J., Lamarque, J.-F., Vitt, F., Schmidt, A., and Gettelman, A.: Radiative and chemical response
770 to interactive stratospheric sulfate aerosols in fully coupled CESM1 (WACCM), *J. Geophys.
771 Res.*, 122, 13061–13078, <https://doi.org/10.1002/2017JD027006>, 2017.

772 Murphy, D. M., Froyd, K. D., Bourgeois, I., Brock, C. A., Kupc, A., Peischl, J., Schill, G. P.,
773 Thompson, C. R., Williamson, C. J., and Yu, P.: Radiative and chemical implications of the
774 size and composition of aerosol particles in the existing or modified global stratosphere,
775 *Atmos. Chem. Phys.*, 21, 8915-8932, 10.5194/acp-21-8915-2021, 2021.

776 Murray, L. T., Jacob, D. J., Logan, J. A., Hudman, R. C., & Koshak, W. J.: Optimized regional
777 and interannual variability of lightning in a global chemical transport model constrained by
778 LIS/OTD satellite data. *Journal of Geophysical Research: Atmospheres*, 117(D20), 2012.

779 Nadykto, A. B., & Yu, F.: Simple correction to the classical theory of homogeneous nucleation.
780 *The Journal of chemical physics*, 122(10), 104511, 2005.

781 NASEM: *Reflecting Sunlight: Recommendations for Solar Geoengineering Research and
782 Research Governance*. Washington, DC: The National Academies Press, 2021.

783 Pye, H. O., & Seinfeld, J. H.: A global perspective on aerosol from low-volatility organic
784 compounds. *Atmospheric Chemistry and Physics*, 10(9), 4377-4401, 2010.

785 Richter, J., Visioni, D., MacMartin, D., Bailey, D., Rosenbloom, N., Lee, W., Tye, M., and
786 Lamarque, J.-F.: Assessing Responses and Impacts of Solar climate intervention on the Earth
787 system with stratospheric aerosol injection (ARISE-SAI), *EGUspHERE* [preprint],
788 <https://doi.org/10.5194/egusphere-2022-125>, 2022.

789 Rotman, D. A., Tannahill, J. R., Kinnison, D. E., Connell, P. S., Bergmann, D., Proctor, D., ... &
790 Kawa, S. R.: Global Modeling Initiative assessment model: Model description, integration,
791 and testing of the transport shell. *Journal of Geophysical Research: Atmospheres*, 106(D2),
792 1669-1691, 2001.

793 Shepherd, J. G.: *Geoengineering the climate: science, governance and uncertainty*. Royal Society,
794 2009.

795 Shi, Q., Jayne, J. T., Kolb, C. E., Worsnop, D. R., & Davidovits, P.: Kinetic model for reaction of
796 ClONO₂ with H₂O and HCl and HOCl with HCl in sulfuric acid solutions. *Journal of
797 Geophysical Research: Atmospheres*, 106(D20), 24259-24274, 2001.

798 Stettler, M.E.J., S. Eastham, S.R.H. Barrett (2011), Air quality and public health impacts of UK
799 airports. Part I: Emissions, *Atmos. Environ.*, 45, 5415-5424, 2011.

800 Stier, P., Feichter, J., Kinne, S., Kloster, S., Vignati, E., Wilson, J., Ganzeveld, L., Tegen, I.,
801 Werner, M., Balkanski, Y., Schulz, M., Boucher, O., Minikin, A., and Petzold, A.: The
802 aerosol-climate model ECHAM5-HAM, *Atmos. Chem. Phys.*, 5, 1125–1156,
803 <https://doi.org/10.5194/acp-5-1125-2005>, 2005.

804 Sun, H., Eastham, S., & Keith, D.: Developing a Plume-in-Grid model for plume evolution in the
805 stratosphere. *Journal of Advances in Modeling Earth Systems*, 14, e2021MS002816.
806 <https://doi.org/10.1029/2021MS002816>, 2022.

807 Svensmark, J., Shaviv, N. J., Enghoff, M. B., & Svensmark, H.: The ION-CAGE code: A
808 numerical model for the growth of charged and neutral aerosols. *Earth and Space Science*, 7,
809 e2020EA001142. <https://doi.org/10.1029/2020EA001142>, 2020.

810 Thompson, C.R., Wofsy, S.C., Prather, M.J., Newman, P.A., Hanisco, T.F., Ryerson, T.B., Fahey,
811 D.W., Apel, E.C., Brock, C.A., Brune, W.H., Froyd, K., Katich, J.M., Nicely, J.M., Peischl,
812 J., Ray, E., Veres, P.R., Wang, S., Allen, H.M., Asher, E., Bian, H., Blake, D., Bourgeois, I.,
813 Budney, J., Bui, T.P., Butler, A., Campuzano-Jost, P., Chang, C., Chin, M., Commane, R.,
814 Correa, G., Crounse, J.D., Daube, B., Dibb, J.E., DiGangi, J.P., Diskin, G.S., Dollner, M.,
815 Elkins, J.W., Fiore, A.M., Flynn, C.M., Guo, H., Hall, S.R., Hannun, R.A., Hills, A., Hintsa,
816 E.J., Hodzic, A., Hornbrook, R.S., Huey, L.G., Jimenez, J.L., Keeling, R.F., Kim, M.J., Kupc,
817 A., Lacey, F., Lait, L.R., Lamarque, J.-F., Liu, J., McKain, K., Meinardi, S., Miller, D.O.,
818 Montzka, S.A., Moore, F.L., Morgan, E.J., Murphy, D.M., Murray, L.T., Nault, B.A.,
819 Neuman, J.A., Nguyen, L., Gonzalez, Y., Rollins, A., Rosenlof, K., Sargent, M., Schill, G.,
820 Schwarz, J.P., Clair, J.M.S., Steenrod, S.D., Stephens, B.B., Strahan, S.E., Strode, S.A.,
821 Sweeney, C., Thamis, A.B., Ullmann, K., Wagner, N., Weber, R., Weinzierl, B., Wennberg,
822 P.O., Williamson, C.J., Wolfe, G.M., and Zeng, L. 'The NASA Atmospheric Tomography
823 (ATom) Mission: Imaging the Chemistry of the Global Atmosphere', *Bulletin of the
824 American Meteorological Society*, 103: E761-E90. 2022.

825 Tilmes, S., Mills, M. J., Niemeier, U., Schmidt, H., Robock, A., Kravitz, B., Lamarque, J.-F., Pitari,
826 G., and English, J. M.: A new Geoengineering Model Intercomparison Project (GeoMIP)
827 experiment designed for climate and chemistry models, *Geosci. Model Dev.*, 8, 43–49,
828 <https://doi.org/10.5194/gmd-8-43-2015>, 2015.

829 Turco, R. P., Whitten, R. C., & Toon, O. B.: Stratospheric aerosols: Observation and theory.
830 *Reviews of Geophysics*, 20(2), 233-279. doi: 10.1029/RG020i002p00233, 1982.

831 van der Werf, G. R., J. T. Randerson, L. Giglio, T. T. van Leeuwen, Y. Chen, B. M. Rogers, M.
832 Mu, M. J. E. van Marle, D. C. Morton, G. J. Collatz, R. J. Yokelson, and P. S. Kasibhatla,
833 Global fire emissions estimates during 1997–2016, *Earth Sys. Sci. Data*, 9, 697-720, 2017.

834 van Donkelaar, A., Martin, R.V., Leaitch, W.R., Macdonald, A.M., Walker, T.W., Streets, D.G.,
835 Zhang, Q., Dunlea, E.J., Jimenez, J.L., Dibb, J.E., Huey, L.G., Weber, R., Andreae, M.O.:
836 Analysis of aircraft and satellite measurements from the Intercontinental Chemical Transport
837 Experiment (INTEX-B) to quantify long-range transport of East Asian sulfur to
838 Canada. *Atmospheric Chemistry and Physics*, 8(11), 2999-3014, 2008.

839 Vehkamäki, H., Kulmala, M., Napari, I., Lehtinen, K. E., Timmreck, C., Noppel, M., & Laaksonen,
840 A.: An improved parameterization for sulfuric acid–water nucleation rates for tropospheric
841 and stratospheric conditions. *Journal of Geophysical Research: Atmospheres*, 107(D22),
842 AAC-3. doi: 10.1029/2002JD002184, 2002.

843 Weisenstein, D. K., Visioni, D., Franke, H., Niemeier, U., Vattioni, S., Chiodo, G., Peter, T., and
844 Keith, D. W.: An interactive stratospheric aerosol model intercomparison of solar
845 geoengineering by stratospheric injection of SO₂ or accumulation-mode sulfuric acid
846 aerosols, *Atmos. Chem. Phys.*, 22, 2955–2973, <https://doi.org/10.5194/acp-22-2955-2022>,
847 2022.

848 Williamson, C., Kupc, A., Wilson, J., Gesler, D. W., Reeves, J. M., Erdesz, F., McLaughlin, R., &
849 Brock, C. A.: Fast time response measurements of particle size distributions in the 3-60 nm
850 size range with the nucleation mode aerosol size spectrometer. *Atmospheric Measurement
851 Techniques*, 11(6), 3491-3509. doi:10.5194/amt-11-3491-2018, 2018.

852 Williamson, C. J., Kupc, A., Axisa, D., Bilsback, K. R., Bui, T., Campuzano-Jost, P., Dollner, M.,
853 Froyd, K. D., Hodshire, A. L., Jimenez, J. L., Kodros, J. K., Luo, G., Murphy, D. M., Nault,
854 B. A., Ray, E. A., Weinzierl, B., Wilson, J. C., Yu, F. Q., Yu, P. F., Pierce, J. R., and Brock,
855 C. A.: A large source of cloud condensation nuclei from new particle formation in the tropics,
856 *Nature*, 574, 399–403, <https://doi.org/10.1038/s41586-019-1638-9>, 2019.

857 Williamson, C. J., Kupc, A., Rollins, A., Kazil, J., Froyd, K. D., Ray, E. A., Murphy, D. M., Schill,
858 G. P., Peischl, J., Thompson, C., Bourgeois, I., Ryerson, T. B., Diskin, G. S., DiGangi, J. P.,
859 Blake, D. R., Bui, T. P. V., Dollner, M., Weinzierl, B., and Brock, C. A.: Large hemispheric
860 difference in nucleation mode aerosol concentrations in the lowermost stratosphere at mid-
861 and high latitudes, *Atmos. Chem. Phys.*, 21, 9065–9088, <https://doi.org/10.5194/acp-21-9065-2021>, 2021.

862 Wofsy, S.C., S. Afshar, H.M. Allen, E.C. Apel, E.C. Asher, B. Barletta, J. Bent, H. Bian, B.C.
863 Biggs, D.R. Blake, N. Blake, I. Bourgeois, C.A. Brock, W.H. Brune, J.W. Budney, T.P. Bui,
864 A. Butler, P. Campuzano-Jost, C.S. Chang, M. Chin, R. Commane, G. Correa, J.D. Crounse,
865 P. D. Cullis, B.C. Daube, D.A. Day, J.M. Dean-Day, J.E. Dibb, J.P. DiGangi, G.S. Diskin,
866 M. Dollner, J.W. Elkins, F. Erdesz, A.M. Fiore, C.M. Flynn, K.D. Froyd, D.W. Gesler, S.R.
867 Hall, T.F. Hanisco, R.A. Hannun, A.J. Hills, E.J. Hintska, A. Hoffman, R.S. Hornbrook, L.G.
868 Huey, S. Hughes, J.L. Jimenez, B.J. Johnson, J.M. Katich, R.F. Keeling, M.J. Kim, A. Kupc,
869 L.R. Lait, K. McKain, R.J. McLaughlin, S. Meinardi, D.O. Miller, S.A. Montzka, F.L. Moore,
870 E.J. Morgan, D.M. Murphy, L.T. Murray, B.A. Nault, J.A. Neuman, P.A. Newman, J.M.
871 Nicely, X. Pan, W. Paplawsky, J. Peischl, M.J. Prather, D.J. Price, E.A. Ray, J.M. Reeves, M.
872 Richardson, A.W. Rollins, K.H. Rosenlof, T.B. Ryerson, E. Scheuer, G.P. Schill, J.C.
873 Schroder, J.P. Schwarz, J.M. St.Clair, S.D. Steenrod, B.B. Stephens, S.A. Strode, C. Sweeney,
874 D. Tanner, A.P. Teng, A.B. Thamis, C.R. Thompson, K. Ullmann, P.R. Veres, N.L. Wagner,
875 A. Watt, R. Weber, B.B. Weinzierl, P.O. Wennberg, C.J. Williamson, J.C. Wilson, G.M.
876 Wolfe, C.T. Woods, L.H. Zeng, and N. Vieznor. 2021. ATom: Merged Atmospheric
877 Chemistry, Trace Gases, and Aerosols, Version 2. ORNL DAAC, Oak Ridge, Tennessee,
878 USA. <https://doi.org/10.3334/ORNLDAA/1925>.

879 Yu, F., & Luo, G.: Simulation of particle size distribution with a global aerosol model: contribution
880 of nucleation to aerosol and CCN number concentrations. *Atmospheric Chemistry and
881 Physics*, 9(20), 7691-7710, 2009.

882 Yu, F., & Turco, R. P.: Ultrafine aerosol formation via ion-mediated nucleation. *Geophysical
883 Research Letters*, 27(6), 883-886. doi: 10.1029/1999GL011151, 2000.

884

885 Yu, F., Nadykto, A. B., Herb, J., Luo, G., Nazarenko, K. M., & Uvarova, L. A.: $\text{H}_2\text{SO}_4\text{--H}_2\text{O--NH}_3$
886 ternary ion-mediated nucleation (TIMN): kinetic-based model and comparison with CLOUD
887 measurements. *Atmospheric Chemistry and Physics*, 18(23), 17451-17474, 2018.

888 Yu, F., Nadykto, A. B., Luo, G., & Herb, J.: $\text{H}_2\text{SO}_4\text{--H}_2\text{O}$ binary and $\text{H}_2\text{SO}_4\text{--H}_2\text{O--NH}_3$ ternary
889 homogeneous and ion-mediated nucleation: lookup tables version 1.0 for 3-D modeling
890 application. *Geoscientific Model Development*, 13(6), 2663-2670, 2020.

891 Zhang, R., Khalizov, A., Wang, L., Hu, M., & Xu, W.: Nucleation and growth of nanoparticles in
892 the atmosphere. *Chemical reviews*, 112(3), 1957-2011, 2012.

893